



Indium-activated bismuth-based catalysts for efficient electrocatalytic synthesis of urea

Yini Mao^a, Yong Jiang^a, Qiao Gou^a, Shengmei Lv^a, Zuyou Song^a, Yimin Jiang^a, Wenbin Wang^a, Ming Li^a, Lirong Zheng^{b,*}, Wei Su^{c,*}, Rongxing He^{a,*}

^a Key Laboratory of Luminescence Analysis and Molecular Sensing (Southwest University), Ministry of Education, College of Chemistry and Chemical Engineering, Southwest University, Chongqing 400715, China

^b Synchrotron Radiation Facility, Institute of High Energy Physics, Chinese Academy of Science, Beijing 100049, China

^c Key Laboratory of Beibu Gulf Environment Change and Resources Utilization (Nanning Normal University), Ministry of Education, College of Chemistry and Life Science, Nanning Normal University, 175 Mingxiu East Road, Nanning 530000, China



ARTICLE INFO

Keywords:

Bi:In/C NPs

Activator

C-N coupling reaction

Urea

ABSTRACT

Urea is of great importance for the survival and development of mankind because of its advantages in effectively increasing crop yields. A novel carbon-supported indium-doped bismuth nanoparticles (Bi: 10 %In/C NPs) was prepared for the synthesis of urea via the co-activated reduction of nitrate and CO₂ with an average Faraday efficiency (FE) of 20.31 % and urea yield (R_{urea}) of 606.38 µg mg⁻¹ h⁻¹. Interestingly, the In doped here not only serves as the active site, but also acts as an activator to stimulate the activity of Bi through electronic interaction, thus making Bi also the active site for the electrocatalytic C-N coupling reaction. Simultaneously, the key intermediates of the reaction are revealed to be *NH₂ and *CO. This work provides further insight into the role of indium in the electrocatalytic C-N coupling for the synthesis of urea, which gives a direction for thinking about the design and construction of subsequent highly efficient electrocatalysts.

1. Introduction

As the most commonly used nitrogen fertilizer with the highest nitrogen content, urea is indispensable for human survival and development [1,2]. However, the industrial synthesis of urea usually takes place under harsh conditions and is accompanied by extremely high energy consumption (N₂ + H₂ → NH₃, 150 ~ 350 bar, 350–550 °C; NH₃ + CO₂ → CO(NH₂)₂, 150–250 bar, 150–200 °C), which significantly exacerbates the energy crisis and environmental problems [3,4]. As a result, electrocatalytic C-N coupling for the synthesis of urea is gradually evolving into an efficient green synthesis method, which is driven by renewable electricity in the premise of applying a suitable catalyst. In this way, two energy-intensive and polluting industrial steps are optimized into a simple and renewable energy-driven electrocatalytic process [5]. Accordingly, the choice of carbon and nitrogen sources has naturally attracted the attention of many researchers. On the one hand, the greenhouse effect caused by the massive emissions of CO₂ leads to global warming, which brings about many and even more environmental problems, such as melting glaciers, heat waves and super storms [6,7]. The resourceful use of abundant CO₂ molecules through

electrocatalytic activation and immobilization not only alleviates the energy shortage, but also contributes to the goal of “carbon neutrality”, which is a necessary practice for the sustainable development of human society [8]. On the other hand, the uncontrolled discharge of municipal and industrial wastewater and the extensive use of pesticides and fertilizers lead to high NO₃/NO₂ concentrations in polluted water, which cause serious environmental damage and human diseases such as blue baby syndrome, non-Hodgkin lymphoma and hypertension [9]. Compared with the harmless treatment of NO₃/NO₂ to nitrogen, the reduction of NO₃/NO₂ to valuable chemicals through electrochemistry for “waste to wealth” is shown to be more attractive [10]. Therefore, the use of CO₂ and NO₃/NO₂ as the carbon and nitrogen source respectively for the electrocatalytic synthesis of urea is of great significance, as it provides a viable solution to both the aforementioned problems of resource utilization of CO₂ and wastewater treatment. Of course, the choice of nitrogen source is not limited to NO₃/NO₂, there are abundant researches on N₂ [11–13] and the fixation of N₂ is of great interest [14, 15], and a comprehensive review of electrocatalytic synthesis of urea was carried out by Jiang and co-workers [16]. However, based on the aforementioned considerations, NO₃/NO₂ is still chosen as the nitrogen

* Corresponding authors.

E-mail addresses: zhenglr@ihep.ac.cn (L. Zheng), suwmail@163.com (W. Su), herx@swu.edu.cn (R. He).

source in this work. The production of urea by electrocatalytic co-reduction of CO₂ and NO₃/NO₂ was first reported by Shibata et al. [17–20] and subsequently explored by many other researchers (summarized in Table S1) [21–25], and the related research work progressed quite rapidly. However, the reduction reaction of NO₃/NO₂ to urea involves a sixteen/fourteen-electron transfer process, which leads directly to the diversity of by-products and the complexity of the reaction mechanism [26]. At present, the reaction mechanism for urea production is still controversial, the possible intermediates and active sites for the reaction are also uncertain [27]. Moreover, it is of great significance to reasonably design and synthesize catalysts for efficient electrocatalytic preparation of urea, which is also the focus and difficulty in this field [24]. Earth-abundant bismuth has the advantages of low price, low toxicity and environmental friendliness. Most importantly, it can effectively activate nitrogen-containing molecules while showing extremely poor hydrogen evolution reaction (HER) activity, and Bi-based catalysts have made some breakthrough recently in the field of carbon dioxide reduction reaction (CO₂RR) and nitrate reduction reaction (NO₃RR). With the inhibition of competitive HER by bismuth, it is of great relevance to design a Bi-based catalyst capable of simultaneously activating carbon dioxide molecules and nitrate for the synthesis of urea [28–32].

In this work, we report a facilely prepared Bi:In/C catalyst for the highly efficient co-reduction of CO₂ and nitrate to synthesize urea in a gas-tight H-type electrolytic cell using a conventional three-electrode system, and propose a rational reaction mechanism. Strikingly, unlike the previously reported In(OH)₃ [25], InOOH [33] and graphene-In₂O₃ [34] indium-based materials, in addition to acting directly as the active site for the C-N coupling reaction, In in the Bi:In/C also affects the reaction indirectly by activating the catalytic activity of Bi through electronic interactions. Of particular interest is the fact that the pure Bi catalyst itself is not active for urea synthesis under the same experimental investigation, but the doping of indium alters this phenomenon, allowing Bi to be activated and become the active sites for the C-N coupling reaction. This work provides some perspective on the role of In in indium-containing catalysts and may also serve as a basis for subsequent studies on Bi-based catalysts.

2. Experimental section

2.1. Materials and chemicals

Sodium borohydride (NaBH₄, AR), sodium hydroxide (NaOH, 98 %), ammonium chloride (NH₄Cl, 99.99 %), potassium nitrate (KNO₃, 99.99 %), potassium nitrate-15 N (K¹⁵NO₃, 99 atom %, ≥ 99.0 %), potassium nitrite (KNO₂, 99.99 %), potassium bicarbonate (KHCO₃, 99.99 %), potassium sulfate (K₂SO₄, 99.99 %), indium chloride tetrahydrate (InCl₃·4 H₂O, 99.5 %), urea-¹⁵N₂ (CH₄¹⁵N₂O, ≥ 98.5 %) and urea (CH₄N₂O, 99 %) were purchased from Shanghai Aladdin Biochemical Technology Co. Ltd.; hydroxylamine (NH₂OH, 50 %) and Nafion (5 wt %) were derived from Sigma-Aldrich; ethanol (C₂H₆O, AR), nitric acid (HNO₃, 65–68 %), sodium citrate (C₆H₅Na₃O₇, ≥ 99 %), bismuth(III) chloride (BiCl₃, 99.9 %) and XC-72R were purchased from Chuandong Chemical Reagents Company (China); carbon paper (CP) was purchased from Shanghai Hesen Electric Co. Ltd; carbon dioxide (CO₂, 99.99 %) was purchased from Chongqing Titanium New Chemical Co. Ltd. All reagents were directly used without further purification.

2.2. Pre-treatment of CP

The CP was cut to the size of 2 cm × 3 cm and placed into a 100 mL reactor with an appropriate amount of concentrated nitric acid, and then kept at 120 °C for 3 h. At the end of the process, the CP was allowed to cool naturally to room temperature, then washed several times with deionised water and anhydrous ethanol in turn, dried at 60 °C for 12 h, and finally removed and cut to 1 cm × 1 cm size for subsequent use.

2.3. Synthesis of catalysts

For Bi:x %In/C (x = 0, 5, 10, 15, 20) (the x % here represents the molar ratio of indium species to bismuth species in the initial feed), 1.1764 g (4 mmol) of C₆H₅Na₃O₇·2H₂O was added to a conical flask containing 100 mL of deionized water, allowed to dissolve and mix thoroughly and then the specified molar ratios of BiCl₃ and InCl₃·4H₂O were added. After stirring for 0.5 h, 0.05 g of XC-72R was added to the mixture and sonicated for 30 min, followed by the dropwise addition of 0.1 mol/L NaBH₄ solution under appropriate stirring speed conditions and stirring overnight after the operation was completed. Finally, the corresponding catalysts were obtained by filtration, washing and drying under vacuum at 60 °C for 12 h.

2.4. Characterization

Physical identification and morphological analysis were carried out by X-ray diffraction (XRD, Bruker D8 Advance) and scanning electron microscopy (SEM, Flex SEM 1000), respectively. Transmission electron microscopy (TEM) and high-resolution transmission electron microscopy (HRTEM) images were obtained on the Talos F200X (FEI). X-ray photoelectron spectroscopy (XPS) and ICP-OES were separately collected on Thermo Scientific K-Alpha and Thermo ICAP PRO equipment. The surface area of the catalysts was determined by surface area & pore size analyzer (QUADRASORB SI), the characterization of defects was carried out by Electron Paramagnetic Resonance Spectrometer (Bruker, EMXplus-9.5/12). The XAFS data was gathered at 1W1B station in Beijing Synchrotron Radiation Facility with storage rings operated at 2.5 GeV with an average current of 250 mA. The samples need to be pre-treated before testing, i.e. diluted with dimethylimidazole, milled well and then pressed into thin slices using a tablet press (YP-3, P = 0.332Q). The EXAFS data obtained were processed according to standard procedures using the ATHENA module as well as the ARTEMIS module of the IFEFFIT software packages so as to evaluate the EXAFS contributions of the different coordination shells and to obtain quantitative structural parameters around the central atom. And ultraviolet-visible (UV-Vis) spectra were obtained by testing on TU-1901 (Beijing General analysis Instrument Co., Ltd.).

2.5. Preparation of working electrode

5.0 mg of catalyst, 400 μL H₂O, 580 μL EtOH and 20 μL Nafion solution were mixed and sonicated for 15 min to prepare a homogeneous ink. Then, 30 μL (7.5 μL × 4 times) of homogeneous ink was evenly distributed onto a hydrophilic CP with an area of 1.0 cm² to obtain the working electrode with an average load mass of 0.15 mg cm⁻². The average loading mass of the catalyst was calculated as: (5 mg × 7.5 μL × 4/1000 μL)/1.0 cm² = 0.15 mg·cm⁻².

2.6. Electrochemical measurement

All electrochemical measurements were performed on CHI 760E workstation. A conventional three-electrode system with a platinum wire as counter electrode and Ag/AgCl/saturated KCl as reference was used for the tests in a well gas-tight H-type electrolytic cell with a mixture of 15 mL KHCO₃ (0.1 M) and 5 mL KNO₃ (0.1 M) as electrolyte, and CO₂ was continuously drummed in at a flow rate of 32 SCCM during the electrolysis. All potentials were converted to the RHE scale using the following equation:

$$E \text{ (vs. RHE)} = E \text{ (vs. Ag/AgCl)} + 0.197 \text{ V} + 0.0591 \times \text{pH} \quad (1)$$

The gas phase products were quantified by on-line gas chromatography with a flame ionization detector (FID) for CO and CH₄, and a thermal conductivity detector (TCD) for N₂, H₂, O₂ quantification. The liquid phase products were quantified by corresponding colorimetric methods. It is worth noting that urea was measured indirectly. The

concentration of NH_3 in the original electrolyte (C_{original}) was measured first, then urea was decomposed by urease ($2(\text{NH}_2)_2\text{CO} \rightarrow \text{CO}_2 + 2\text{NH}_3$), and the concentration of NH_3 in the electrolyte after decomposition reaction (C_{total}) was measured. Finally, the concentration of urea was calculated according to $C_{\text{urea}} = (C_{\text{total}} - C_{\text{original}})/2$. And the FE was calculated by the equation:

$$\text{FE} = \frac{n \times F \times C \times V}{M \times Q} \times 100\% \quad (2)$$

where n represents the number of electrons transferred ($n_{\text{urea}} = 16$, $n_{\text{NH}_3} = 8$, $n_{\text{NH}_2\text{OH}} = 6$, and $n_{\text{NO}_2} = 2$), F is the Faraday constant ($96485 \text{ C} \cdot \text{mol}^{-1}$), C represents the concentration of each product measured in the experiment ($\mu\text{g} \cdot \text{mL}^{-1}$), V represents the total volume of the catholyte (mL), M represents the molecular weight ($M_{\text{urea}} = 60.06$, $M_{\text{NH}_3} = 17$, $M_{\text{NH}_2\text{OH}} = 33$ and $M_{\text{NO}_2} = 46 \text{ g} \cdot \text{mol}^{-1}$) and Q is the total charge (C).

The formation rate (R) of each product was calculated by the following formula:

$$R = \frac{C \times V}{t \times m} \quad (3)$$

where C and V are the same as before, t represents the duration of the electrocatalysis test (h) and m represents the catalyst loading (mg).

2.7. Isotope labeling experiments

K^{15}NO_3 was used instead of KNO_3 as the feeding N-source for isotope labelling experiments. Firstly, the electrolyte after the i-t test was lyophilized; then 2 mL of dichloromethane (CH_2Cl_2) was added to the solid obtained, dissolved and the supernatant was taken and placed in a fume cupboard to allow all of the CH_2Cl_2 to evaporate, and lastly, the sample obtained was dissolved in 0.6 mL of deuterium chloroform (CDCl_3) and sonicated for 15 min before being used for NMR detection.

2.8. Density functional theory (DFT) calculations

All DFT calculations were performed by Vienna ab initio simulation package (VASP). The projector augmented wave (PAW) potentials with a planewave cutoff energy of 450 eV were employed to calculate the interaction between the ionic cores and valence electrons [35]. The generalized gradient approximation (GGA) functional of Perdew-Burke-Ernzerhof (PBE) functional was applied as the exchange-correlation functional [36]. The $2 \times 2 \times 1$ Gamma-centered k-points grid was used to sample the Brillouin zone. The model is not fixed during the calculation, the convergence thresholds were set as 10^{-5} eV for the energy and $0.02 \text{ eV} \cdot \text{\AA}^{-1}$ for the force. The energy barriers of transition states for the key intermediates were calculated by the

binding image nudged elastic band (CI-NEB) method, the energy convergence thresholds were set as $1 \times 10^{-7} \text{ eV}$ and the force convergence thresholds were less than $0.05 \text{ eV} \cdot \text{\AA}^{-1}$. Here, Bi (012) slab was modeled and calculated. The adsorption energy and Gibbs free energy were calculated as follows :

$$\Delta E_{\text{ads}} = E_{\text{sur}-M} - E_{\text{sur}} - E_M \quad (4)$$

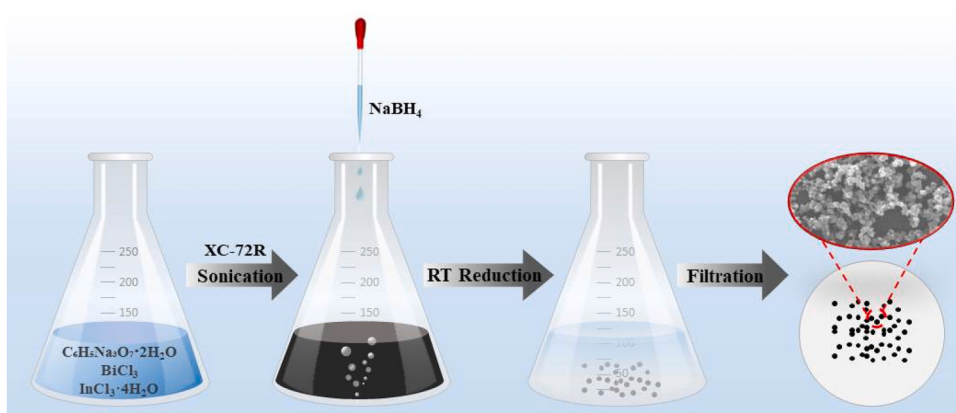
$$G = E_{\text{DFT}} + E_{\text{ZPE}} - TS \quad (5)$$

3. Results and discussion

3.1. Structural characterization

The Bi:10 %In/C NPs were prepared by a simple room temperature reduction method using sodium citrate and sodium borohydride as auxiliary and reducing agent [37], respectively (see Experimental section and Scheme 1 for details). Fig. 1a shows the XRD patterns of Bi:10 %In/C, Bi/C and In/C. Bi/C and In/C samples show Bi peaks (JCPDS 44-1246) and In peaks (JCPDS 65-9682), respectively, indicating that the as-prepared Bi/C and In/C are crystalline, although the crystallinity of the In/C appears to be significantly lower than that of the Bi/C. Three characteristic diffraction peaks for Bi:10 %In/C appeared at $2\theta = 27.49^\circ$, 38.25° and 39.89° are significantly shifted towards higher angles compared to Bi/C (27.18° , 37.95° and 39.62°), without any peaks of impurity. Inferentially, In with a smaller radius doped into the site of Bi, causing the shrinkage of Bi lattice and thus leading to a high angular shift of the diffraction peak [38]. Next, a series of samples at other ratios were prepared by varying the feed ratio of In (Fig. S1), and the actual doping proportion of In was measured by ICP-OES and the results are shown in Table S2. As the feed ratio of In continues to increase ($>10\%$), multiple heterogeneous peaks (Fig. S1, marked with purple diamonds) attributed to BiIn alloy (JCPDS 65-3887) gradually appeared, indicating that the Bi lattice has reached the limit of inclusivity.

The field-emission scanning electron microscopy (SEM), transmission electron microscopy (TEM), high-resolution TEM (HRTEM) and high-angle annular dark-field scanning transmission electron microscopy (HAADF-STEM) images of Bi:10 %In/C are shown in Fig. S2a-c and Fig. 1b-d. Evidently, the skeletons of the Bi:10 %In/C sample are composed by a number of nanoparticles with an average particle size of 108.6 nm (Fig. 1b, Fig. S2d), and the well-resolved lattice fringes ($d = 0.327 \text{ nm}$ and $d = 0.228 \text{ nm}$) shown in the HRTEM image indicate that the sample prepared here exposes mainly the (012) and (110) crystal planes of Bi (Fig. 1c). Fig. 1d confirms the presence of the C, In and Bi elements, which are uniformly distributed over the whole catalyst. Meanwhile, the variation of the crystalline spacing Δd was calculated for several main crystalline planes after doping (Table S3), and the results showed that In was mainly doped on the (012) plane.



Scheme 1. Schematic illustration of the Bi: x %In/C NPs synthesis process.

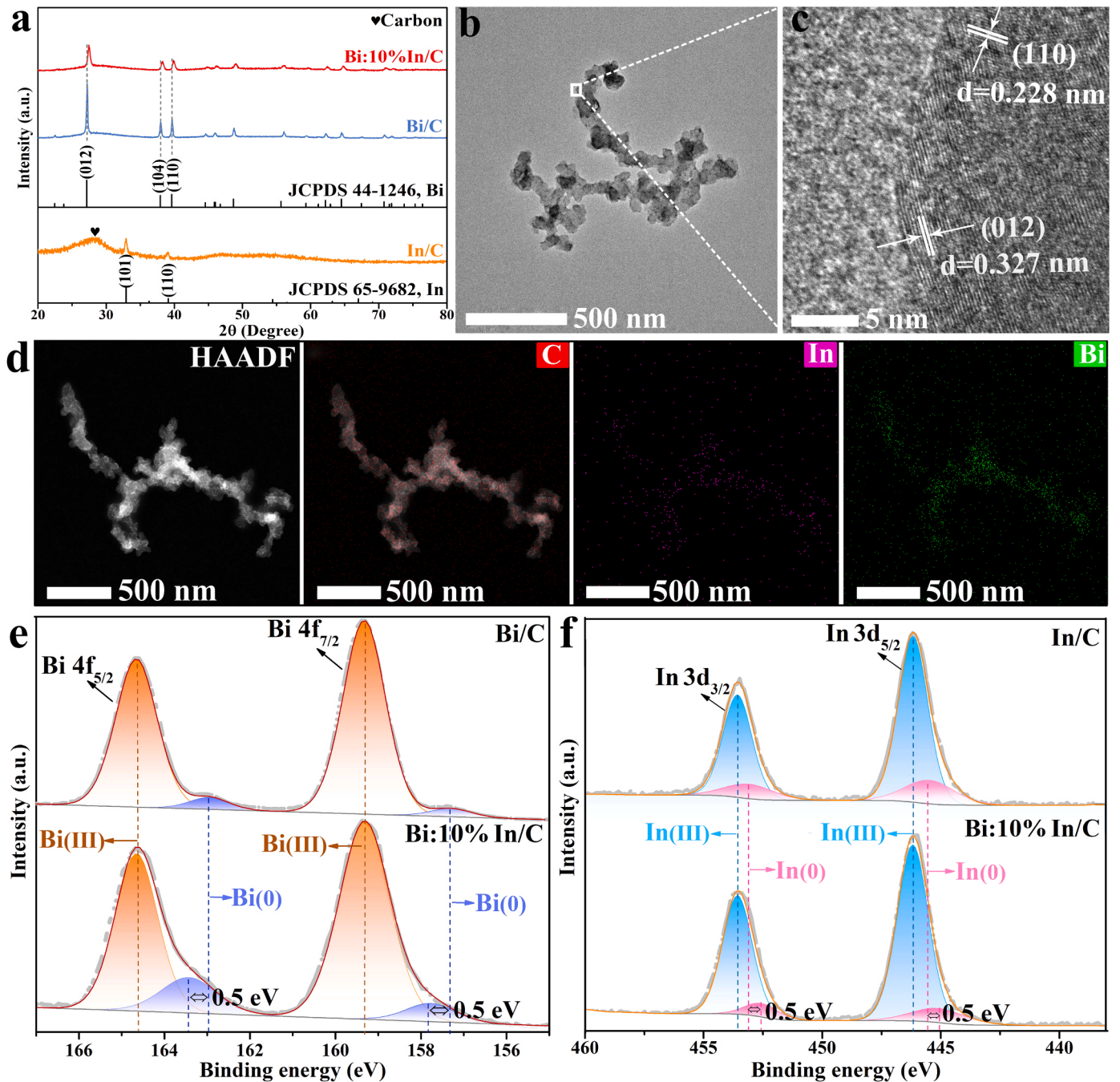


Fig. 1. (a) XRD patterns of Bi:10 %In/C, Bi/C and In/C; TEM (b), HRTEM images (c) and HAADF-STEM (d) images of Bi:10 %In/C with corresponding elemental mappings of C, In and Bi; High-resolution spectra of Bi 4f (e) and In 3d (f).

Immediately afterwards, X-Ray photoelectron spectroscopy (XPS) analysis was carried out to investigate the chemical state of Bi and In in the Bi:10 %In/C and the XPS survey spectrum is shown in Fig. S3. The high-resolution XPS spectra of Bi 4f demonstrates that both Bi⁰ and Bi³⁺ species (trivalent species derived from surface oxidation of non-precious metals) can be detected from Bi:10 %In/C (Fig. 1e), two purple-filled fitted peaks at binding energies of 163.48 eV and 157.78 eV are originate from Bi 4f_{5/2} and Bi 4f_{7/2} of Bi⁰, and two orange-filled fitted peaks at binding energies of 164.68 eV and 159.38 eV are derived from Bi 4f_{5/2} and Bi 4f_{7/2} of Bi³⁺ [39,40]. Compared to pure Bi, the position of the fitted peak corresponding to Bi³⁺ species remains unchanged, but the position of the Bi⁰ species is positively shifted by 0.5 eV.

(For Bi/C, Bi 4f_{5/2}: 162.98 eV, Bi 4f_{7/2}: 157.28 eV). Additionally, the

high-resolution XPS spectra of In 3d also yielded four fitted peaks by peak-fitting analysis (Fig. 1f), indicating the presence of both 0 and +3 valence states of indium in Bi:10 %In/C. Two fitted peaks filled with blue at binding energies of 453.58 eV and 446.18 eV attributed to In 3d_{3/2} and In 3d_{5/2} of In³⁺ species, with no offset compared to pure In; while the other two fitted peaks filled with pink at 452.58 eV and 445.08 eV generated by In 3d_{3/2} and In 3d_{5/2} of In⁰ species are negatively shifted by 0.5 eV (For In/C, In 3d_{3/2}: 453.08 eV; In 3d_{5/2}: 445.58 eV) [41]. The peaks of Bi³⁺ and In³⁺ in Bi:10 %In/C do not show the same shift compared to the peaks of Bi³⁺ and In³⁺ in pure Bi and In, indicating that the shifts of Bi⁰ and In⁰ in Bi:10 %In/C are not caused by systematic errors, but by intrinsic differences in charge, i.e. the blue shift of Bi and the red shift of In are resultant from the electron transfer from

Bi to In [42,43]. The electron interaction here may play an important role in regulating the adsorption energy of CO_2 , nitrate and related intermediates, and can affect the reaction pathway and efficiency of electrocatalytic C-N coupling for the synthesis of urea [44,45].

The fine structure of Bi:10 %In/C and the chemical states of Bi were further investigated using X-ray absorption near edge structure (XANES) and the extended X-ray absorption fine structure (EXAFS) spectra. Fig. 2a shows the Bi L₃-edge XANES of Bi/C, Bi:10 %In/C, Bi:10 %In/C after testing, Bi foil and Bi_2O_3 . It can be found that the spectra in the three samples prepared almost overlap with the Bi foil, indicating that the Bi species are in the Bi^0 state, again demonstrating the successful preparation of In-doped Bi alloy nanoparticles. The absorption threshold position of Bi:10 %In/C shifts slightly to higher energy (inset of Fig. 2a) compared to that of Bi/C, indicating that Bi is in the electron deficient state after doping, which is consistent with the XPS results (Fig. 1e) [46, 47]. The absorption threshold position of Bi:10 %In/C after testing shifts slightly to lower energy compared to that of Bi:10 %In/C before test indicates a reduction in the oxidation state of Bi. These results together indicate that Bi is likely to be the active site for the electrocatalytic reaction [48]. The Fourier transforms of Bi L₃-edge EXAFS is shown in Fig. 2b, the characteristic peaks at $\sim 2.6 \text{ \AA}$ and $\sim 3.0 \text{ \AA}$ are attributed to the intra- and interlayer.

Bi-Bi bonds, respectively, which differ from the theoretical values (3.097 \AA and 3.589 \AA in Fig. 2c) due to the fact that the test results show distances between electron clouds, whereas the theoretical values indicate distances between atomic nucleus. Wavelet transform analysis

further confirmed the difference of Bi-Bi bond distance (Fig. S4). In particular, the interlayer Bi-Bi bond shifts slightly in the direction of reduced bond length after the introduction of In, which effectively promotes the delocalization of Bi p-electrons, thus enhancing the adsorption and activation of reactive species [49]. The occurrence of precisely observable Bi-O bonds around 1.6 \AA is due to oxidation of the material caused by prolonged exposure to air, as well as some Bi_2O_3 clusters and oxygen-containing groups on the surface of the carrier. In addition, the Bi-Bi coordination mode in Bi:10 %In/C is almost identical before and after the test (Fig. 2d), indicating that the catalyst has good stability (This point is more fully discussed later) [49–51].

3.2. Electrocatalytic urea synthesis

The activity of Bi:10 %In/C for the electrocatalytic co-activated reduction of CO_2 and NO_3^- to produce urea was investigated by the chrono-amperometry (CA) method in a gas-tight H-type electrolytic cell using a conventional three-electrode system (Fig. S5). The gas phase and liquid phase products from the electrolysis process were determined by on-line gas chromatography and colorimetric methods respectively (Fig. S6). In this case, urea is detected by the urease decomposition method, which means that it is first decomposed by urease and then indirectly determined by the indophenol blue method, rather than directly by the diacetylmonoxime method (Table S4).

As shown in Fig. 3a, the performance of Bi:10 %In/C electrocatalytic urea synthesis was evaluated over a range of different application

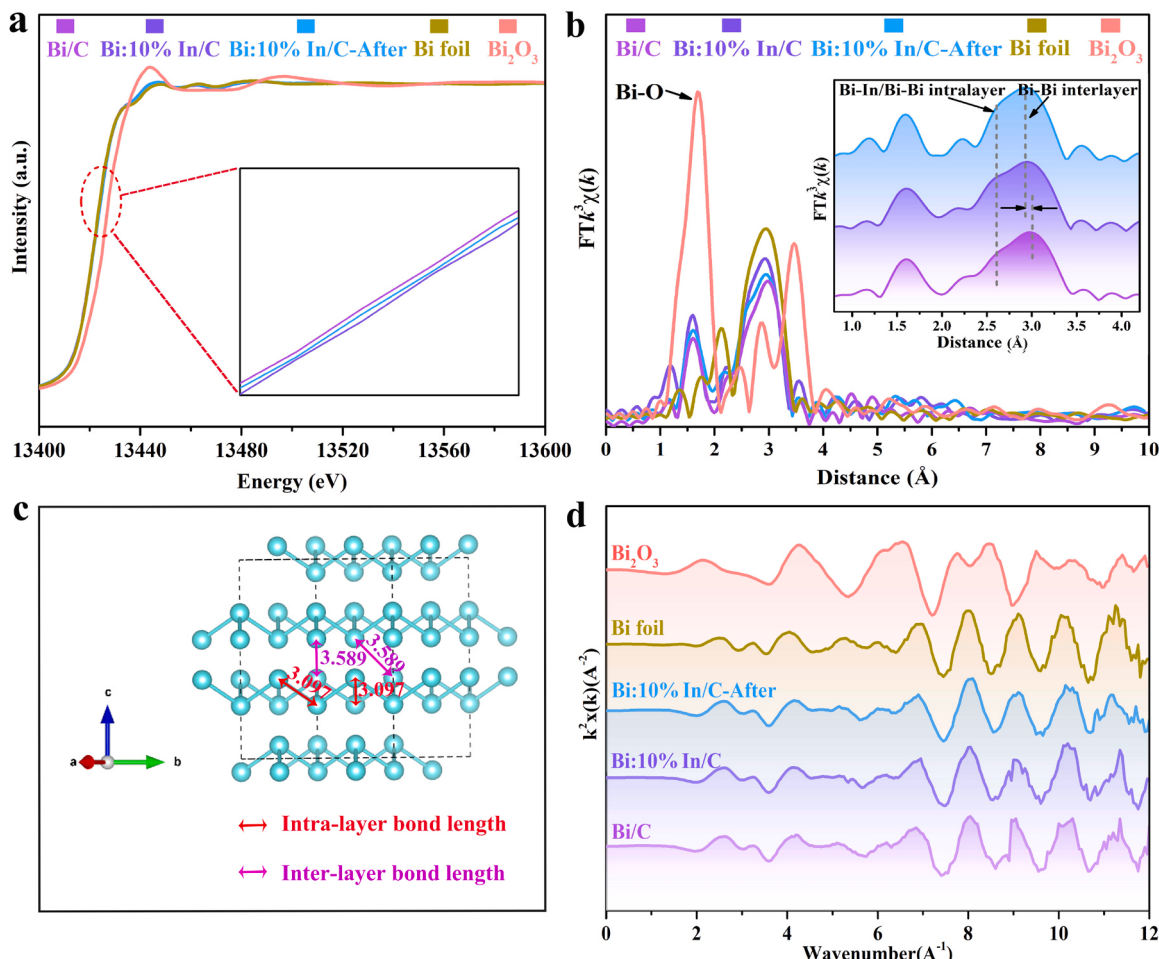


Fig. 2. (a) The normalized XANES spectra at the Bi L₃-edge of Bi/C, Bi:10 %In/C, Bi:10 %In/C after testing, Bi foil and Bi_2O_3 (The inset is a magnified partial view of the red dashed box); (b) R space and corresponding inverse FT-EXAFS results of Bi/C, Bi:10 %In/C, Bi:10 %In/C after testing, Bi foil and Bi_2O_3 (The inset shows a partial enlargement of Bi/C, Bi:10 %In/C and Bi:10 %In/C after testing); (c) The crystal structure of Bi; (d) Bi L₃-edge EXAFS oscillations spectra for Bi/C, Bi:10 %In/C, Bi:10 %In/C after testing, Bi foil and Bi_2O_3 .

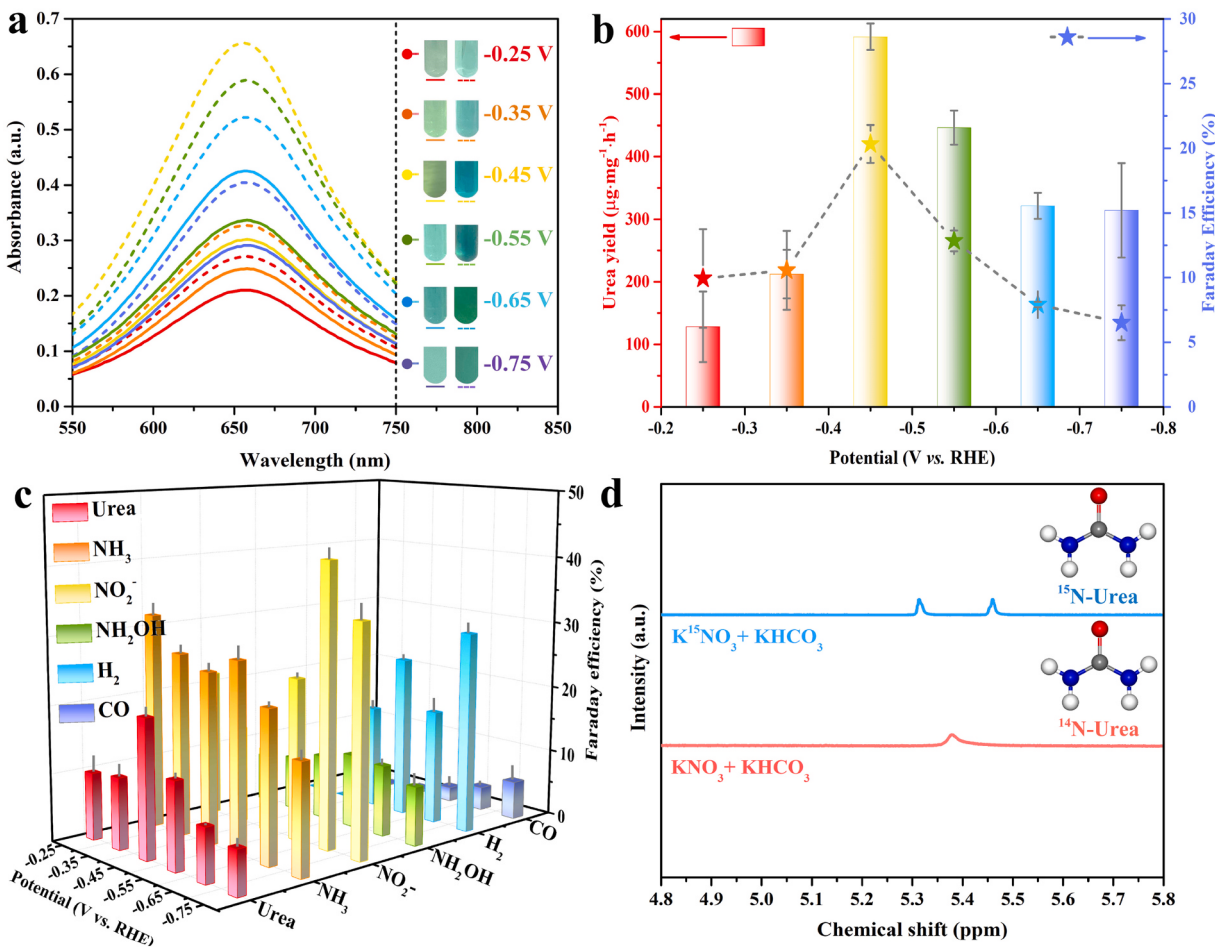


Fig. 3. (a) UV-Vis absorption spectrum of the electrolyte at different potentials ($-0.25 \sim -0.75$ V vs. RHE) after 3600 s electrolysis with continuous CO_2 feeding (The solid and dashed lines indicate the absorbance of NH_3 in the original electrolyte and in the electrolyte after the urease decomposition reaction, and the inset on the right shows the colors at each potential); (b) Corresponding R_{urea} and FE at different potentials; (c) The FE for each species at different potentials ($-0.25 \sim -0.75$ V vs. RHE); (d) ¹H NMR spectra of two electrolytes after electrolysis performance.

potentials from -0.25 to -0.75 V vs. RHE (Fig. S7, repeated three times), both the R_{urea} and FE show a volcanic curve and reach the optimum value of $606.38 \mu\text{g mg}^{-1}\text{h}^{-1}$ and 20.31% (Fig. 3b) at an application potential of -0.45 V vs. RHE. To be noted, the test duration at each potential was experimentally determined to be 1 h (Fig. S8). As the ¹H NMR spectra can be integrated to obtain the content of the corresponding urea, we carried out a quantitative analysis using this method to verify the accuracy of the colourimetric method (Fig. S9). It was found that the urea yields calculated by ¹H NMR spectroscopy were very close to those calculated by the colourimetric method. To increase the feasibility of the data, the same test was carried out by increasing the electrode area (Fig. S10), and the similarity demonstrated the reliability of the experimental data. It has been demonstrated in Fig. S11a-d that the excellent electrocatalytic activity of Bi:10 %In/C is not generated by the surface oxidation component. In addition, the various liquid phase by-products (NH_3 , NO_2 , NH_2OH) generated throughout the electrocatalytic reaction were identified and the gas phase products (CO and H_2) (Fig. S12) were detected by on-line gas chromatography (GC), the distribution of FEs for each species at different potentials is shown in Fig. 3c. Subsequently, several sets of control experiments were carried out to investigate the origin of the N and C elements in urea, and the absence of either NO_3^- or CO_2 resulted in the failure to produce urea (Fig. S13), which ruled out the possibility of contamination of the test system and indicated that urea is indeed produced by the co-activated reduction of NO_3^- and CO_2 , and the isotope labelling experiments verified this conclusion (Fig. 3d, Fig. S14). More importantly, we also

performed quantitative analyses by isotope labelling experiments (Fig. S15a-d), which more strongly proved the accuracy of the above experimental results.

Particularly, the linear scanning voltammetry (LSV) curves, ultraviolet-visible (UV-Vis) absorption spectrum at optimum potential (-0.45 V vs. RHE) and corresponding R_{urea} and FE for Bi:10 %In/C, Bi/C and In/C catalysts are shown respectively in Fig. S16, and it can be observed that the catalytic performance of Bi:10 %In/C is far superior to that of the monometallic electrode (where Bi/C is inactive and In/C shows a general catalytic activity), confirming the excellent performance of Bi:10 %In/C for the electrocatalytic synthesis of urea. Apparently, the excellent catalytic activity of Bi:10 %In/C is very closely related to the doping of In, which is likely to act as the active site for electrocatalytic reactions. To further investigate the role of In, the catalytic activity of Bi: x %In/C ($x = 0, 5, 10, 15, 20$) samples for urea electrocatalytic synthesis was investigated and Fig. S17a-c show the UV-Vis absorption spectra, R_{urea} and FE of each sample. Noteworthily, the catalytic activity increased first and then decreased with the increase of the feed ratio of In, and an optimum R_{urea} of $606.38 \mu\text{g mg}^{-1}\text{h}^{-1}$ and a maximum FE of 20.31% are achieved when the feed ratio of In is 10 %. Combined with the XRD (Fig. S1) results of each sample, a progressive increase in performance is observed with increasing amounts of In before the phase change occurs, followed by a decrease in performance due to the gradual appearance of the BiIn phase, indicating that the BiIn alloy has no positive propulsive effect on the synthesis of urea, and that the catalytic performance is mainly derived from the In-doped Bi

species, of which In is the active site. Furthermore, the BET tests (Fig. S18) were carried out and the Bi:10 %In/C sample showed the largest specific surface area of $127.0 \text{ m}^2 \text{ g}^{-1}$, which undoubtedly allows for more active sites to be exposed and is another contributing factor to the best performance of Bi:10 %In/C.

Further justification is provided for the inference drawn from the XAFS characterisation that Bi may be the active site of the catalyst. As shown in Fig. 4a–c, the adsorption capacity for CO_2 and the reduction capacity for CO_2 and NO_3^- of Bi/C, Bi:10 %In/C, and In/C (also with In^0 as the active site) were compared. It can be found that Bi:10 %In/C has the highest CO_2 adsorption capacity (Fig. 4a), indicating that it may have more active sites for CO_2 adsorption. Bi/C shows no CO_2 reduction activity, while Bi:10 %In/C shows far higher catalytic activity than In/C (Fig. 4b), and for NO_3^- reduction also shows a pattern of Bi:10 %In/C > In/C > Bi/C (Fig. 4c). If only In^0 is used as the active site in Bi:10 %In/C, then the adsorption/reduction capacity for CO_2 .

and the reduction capacity for NO_3^- by In/C with more active sites should be better under the same conditions. Therefore, it is likely that In here also plays the role of activator, activating the catalytic activity of Bi through electron-modulation, thus turning Bi into the active site of the reaction as well. Next, the contents of Bi and In dissolved in the electrolyte after different durations (5 min, 10 min, 15 min, 0.5 h, 1 h, and 12 h) of electrolysis were measured by the ICP-OES and the results are listed in Table S5. It can be seen that the leaching amounts of both In and Bi are small and nearly tends to be stable after 15 min. Interestingly, the percentage of Bi leached during electrolysis is lower than that of In, which has been demonstrated previously as the catalytic active site, further suggesting that Bi also plays an active site role [48].

Next, density functional theory (DFT) calculations were performed to further demonstrate the successful activation of Bi by In, which also becomes the active site for the C-N coupling reaction. Bi (012) slab was modeled and calculated based on TEM result (Fig. 1c) and optimal adsorption configuration (Table S6). The charge density distribution is shown in Fig. 4d, where it can be seen that the In doping leads to a

redistribution of the charge density, with a significant increase around In and a decrease around Bi, which is consistent with the XPS results (Fig. 1e and f). Density of states (DOS) were also carried out to clarify the changes caused by the incorporation of In. As shown in Fig. 4e, the incorporation of In leads to a negative shift in the p -band center of Bi (from -1.02 to -1.35 eV) and an increase in the density of states near the Fermi level (Fig. 4f), which is conducive to improving the electron conductivity and electron transfer ability, and thus enhancing the intrinsic activity of the material [52]. Moreover, the adsorption energy of CO_2 on the Bi (012) surface before and after doping and that of CO_2 at the In site and Bi site after doping were compared (Table S7). The CO_2 adsorption energy is $+0.02$ eV for Bi/C and -0.14 eV for Bi:10 %In/C, indicating that Bi/C has almost no ability to capture CO_2 , which is consistent with Fig. 4a and b. It is worth noting that the CO_2 adsorption energy at the In site is -0.14 eV and at the Bi site is -0.04 eV for Bi:10 %In/C, indicating that the In site is more favourable for CO_2 adsorption, which is the reason for using In as the CO_2 adsorption site in subsequent pathway calculations. Furthermore, the CO_2 adsorption energy at the Bi site changed from $+0.02$ eV in Bi/C to -0.04 eV in Bi:10 %In/C, implying that In actually activates the activity of Bi.

In addition to the excellent electrocatalytic activity, the stability of the electrocatalyst is also pivotal to the practical application. Fig. 5a shows that the crystalline phase of Bi:10 %In/C remains unchanged after electrolysis for different electrolysis durations, which indicates an excellent stability of Bi:10 %In/C. Fig. 5b and c show the CA, FE and R_{urea} results for 14 cycles of testing at the potential of -0.45 V vs. RHE, respectively. After 14 cycles, no sharp drop in activity was observed, again demonstrating the excellent stability of the catalyst. The normalised high-resolution XPS spectra of Bi 4f and In 3d of the catalyst before and after 14 cycles of testing are shown in Fig. 5d and e, it can be observed that the peaks corresponding to Bi^{3+} and In^{3+} weaken considerably after the stability test, which is in consistent with the conclusion of XAFS (Fig. 2a). While the peaks corresponding to Bi^0 and In^0 are still present and relatively enhanced, which indicates that both

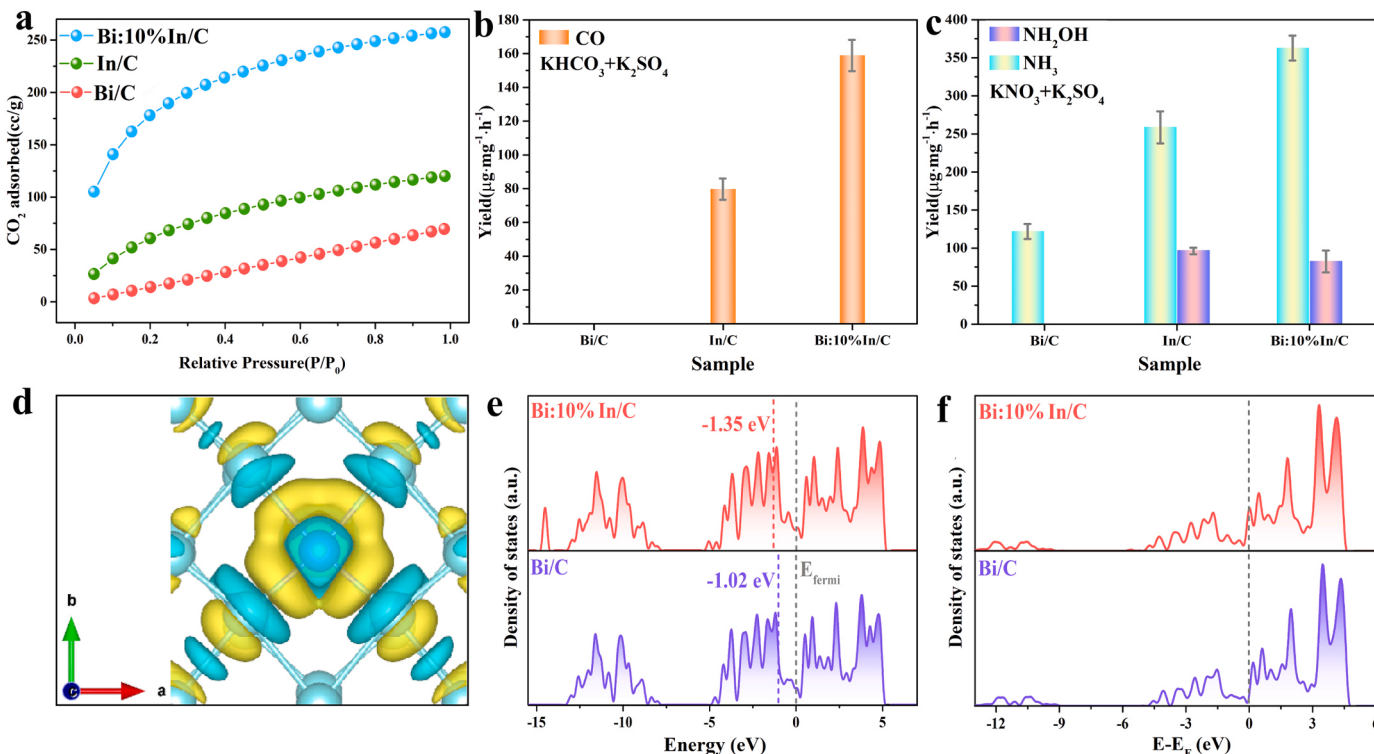


Fig. 4. (a) CO_2 desorption curves; R_{CO} (b), R_{NH_3} and $R_{\text{NH}_2\text{OH}}$ (c) of different samples; (d) Charge density distribution of catalyst (The cyan part indicates a decrease in charge density and the yellow part indicates an increase in charge density); (e) p-band center level of Bi/C and Bi:10 %In/C; (f) PDOS of Bi element for Bi/C and Bi:10 %In/C.

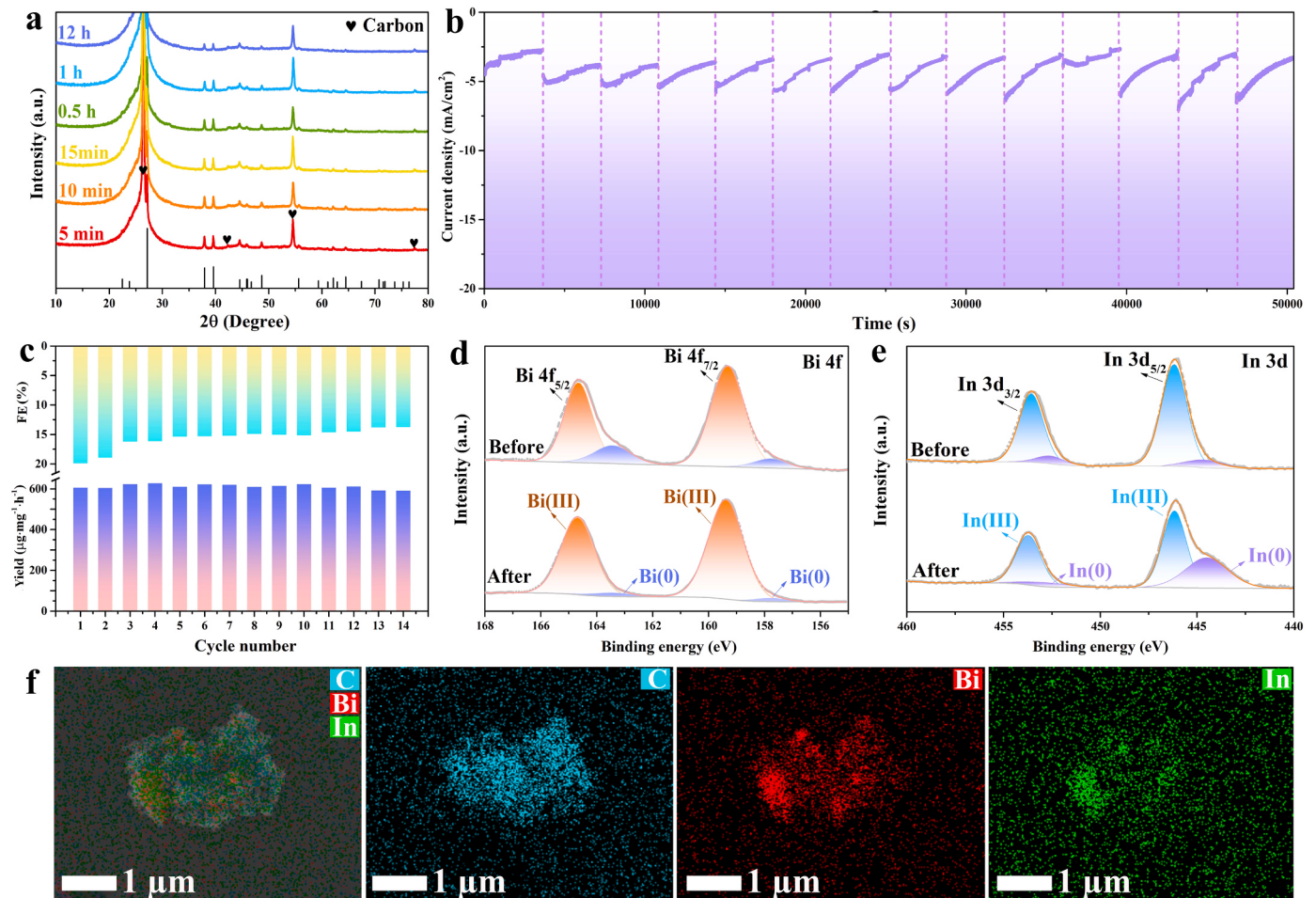


Fig. 5. (a) XRD patterns of Bi:10 %In/C after different durations of electrolysis; (b) CA results of cycling 14 times for Bi:10 %In/C at -0.45 V vs. RHE with continuous CO_2 feeding; FE and R_{urea} (c) of cycling 14 times for Bi:10 %In/C at -0.45 V vs. RHE with continuous CO_2 feeding; High-resolution spectra of Bi 4f (d) and In 3d (e) before and after electrolysis at -0.45 V vs. RHE for 12 h; (f) The element distribution of C, In, Bi of Bi:10 %In/C after electrolysis.

Bi^0 and In^0 should be used as active sites in electrocatalysis and the presence of Bi^0 and In^0 should be favourable for the activity and stability of Bi:10 %In/C [53,54]. Concurrently, the stability tested sample was morphologically characterised and as shown in Fig. S19 and Fig. 5f, the skeletons of Bi:10 % In/C after electrolysis are still composed of many nanoparticles and the elements C, In and Bi are still homogeneously distributed throughout the skeleton, with the only difference being the apparent agglomeration compared to the SEM image of the sample before the test (Fig. S2).

3.3. Mechanism investigation

The mechanism of the electrocatalytic C-N coupling reaction over Bi:10 %In/C catalysts was analyzed. Various mechanisms for the synthesis of urea via electrocatalytic C-N coupling reaction have been reported, mainly including $^{*}\text{CO} + ^{*}\text{NH}_2$, $^{*}\text{CO} + ^{*}\text{NH}_2\text{OH}$, $^{*}\text{CO} + ^{*}\text{NO}$, $^{*}\text{COOH} + ^{*}\text{NH}_2$, $^{*}\text{CO}_2 + ^{*}\text{NO}_2$ and $^{*}\text{CO}_2 + ^{*}\text{NH}_2$ coupling mechanisms [16,23,26,27,55]. In the present work, we propose the coupling mechanism of $^{*}\text{CO} + ^{*}\text{NH}_2$. For $^{*}\text{CO}$, as CO production was detected in the experiment, and urea was also found to be produced when CO was used as the carbon source (Fig. S20), suggesting that CO is one of the key intermediates in the C-N coupling reaction. For $^{*}\text{NH}_2$, as NH_2OH and NH_3 were detected simultaneously in the electrolyte after the electrocatalytic reaction (Fig. S12), a tentative conclusion can be drawn that the $\text{NO}_3 \rightarrow \text{NH}_3$ may prefer to follow the $^{*}\text{NH}_2\text{OH}$ pathway, i.e. $\text{NO}_3 \rightarrow \text{NO}_2 \rightarrow \text{NO} \rightarrow \text{NOH} \rightarrow \text{NHOH} \rightarrow \text{NH}_2\text{OH} \rightarrow \text{NH}_2 \rightarrow \text{NH}_3$ (Fig. S21). When NH_2OH was used as the nitrogen source (Fig. S22)

[56], no urea was found to be produced, indicating that NH_2OH should not be the key intermediate for direct coupling with $^{*}\text{CO}$. Meanwhile, $^{*}\text{NH}_2$ intermediate and C-N bonding were detected by in-situ FIR spectroscopy at 1268 cm^{-1} and 1450 cm^{-1} , respectively (Fig. S23). Therefore, it is speculated that $^{*}\text{NH}_2$ is a key intermediate in urea production, and a more plausible reaction pathway is shown in Fig. S24.

The pathway was further verified by the aid of DFT calculations [57]. Fig. 6a shows the calculated Gibbs free energies of NO_3^- reduction to $^{*}\text{NH}_2$ on Bi:10 %In/C, the optimization models corresponding to each step are shown in Fig. S25. $^{*}\text{NO}_3^-$ undergoes two successive exothermic deoxygenation processes to form $^{*}\text{NO}$, which is then hydrogenated to form $^{*}\text{NHO}$ or $^{*}\text{NOH}$. Apparently, $^{*}\text{NO} \rightarrow ^{*}\text{NHO}$ ($\Delta G =$

$+0.44\text{ eV}$) is less likely to proceed than $^{*}\text{NO} \rightarrow ^{*}\text{NOH}$ ($\Delta G = +0.23\text{ eV}$). And $^{*}\text{NOH} \rightarrow ^{*}\text{NHOH}$ (-0.51 eV) possesses a more negative energy than $^{*}\text{NOH} \rightarrow ^{*}\text{N}$ (-0.29 eV), suggesting that the reduction of NO_3^- on Bi:10 %In/C indeed favors the $^{*}\text{NH}_2\text{OH}$ pathway (Fig. S21). As shown in Fig. 6b, Bi:10 %In/C exhibits an adsorption free energy of -0.80 eV , and the evolution of $^{*}\text{CO}_2 \rightarrow ^{*}\text{COOH} \rightarrow ^{*}\text{CO}$ undergoes two successive proton-coupled electron transfer processes [24], both spontaneous and exothermic with energies of -0.11 and -0.66 eV , respectively, indicating that Bi:10 %In/C is conducive to the reduction of CO_2 . The optimized models of different intermediates of CO_2 reduction to $^{*}\text{CO}$ on Bi:10 %In/C are shown in Fig. S25 [58]. As can be seen from the insets of Fig. 6a and b, both $^{*}\text{NO}_3^-$ and $^{*}\text{CO}_2$ show relatively good electronic interactions with Bi:10 % In/C, which suggests that Bi:10 % In/C is indeed favourable for the adsorption and reduction of NO_3^- and CO_2 . And the PDOS of the Bi element in Bi:10 %In/C before and

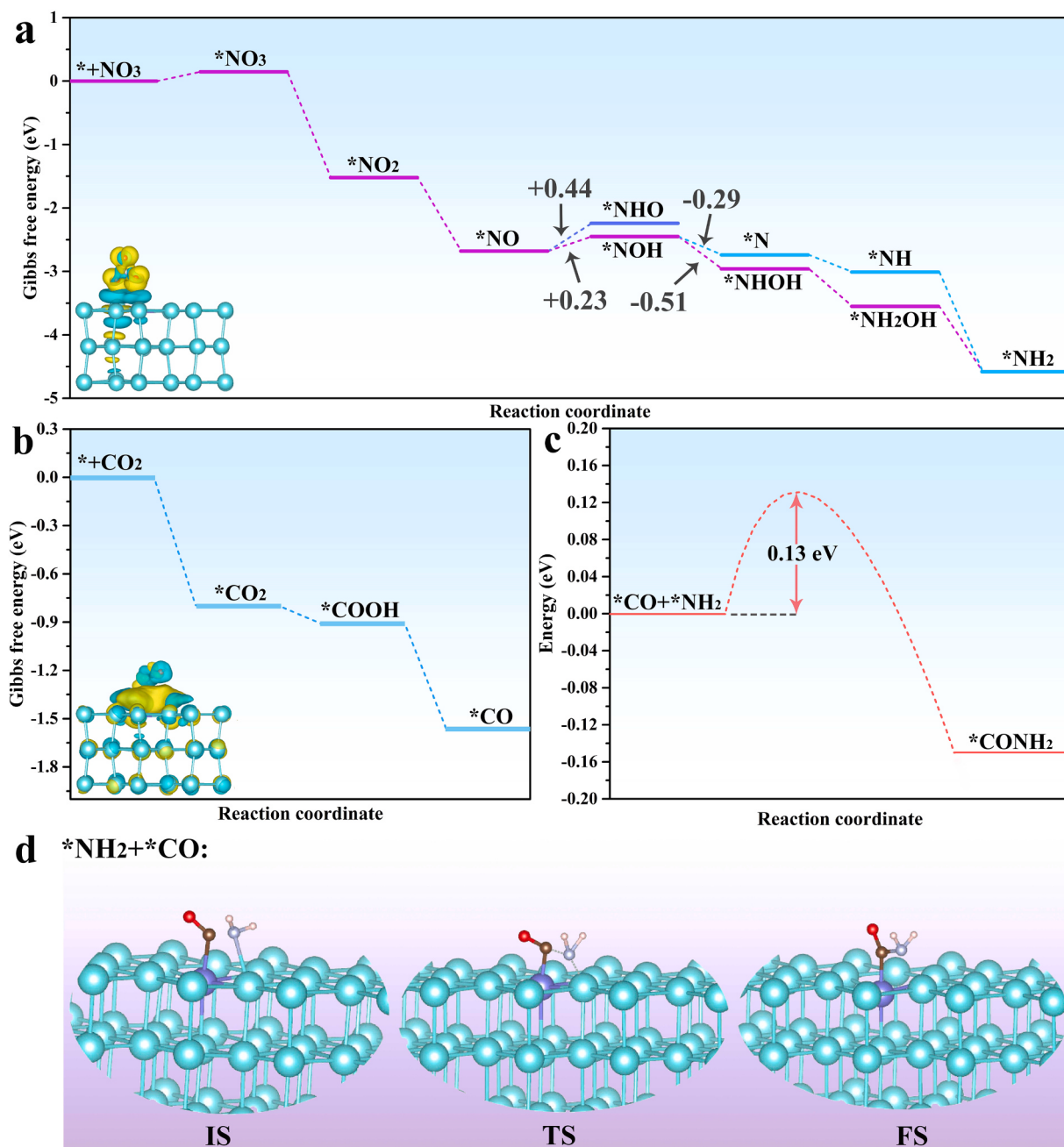


Fig. 6. (a) Calculated Gibbs free energies of NO₃ reduction to *NH₂ on Bi:10 %In/C (The inset shows the charge density differences of *NO₃ on Bi:10 %In/C, yellow and cyan contours represent electron accumulation and depletion, respectively); (b) Calculated Gibbs free energies of CO₂ reduction to *CO on Bi:10 %In/C (The inset shows the charge density differences of *CO₂ on Bi:10 %In/C); (c) Energy barrier in the C-N coupling pathway of *CO and *NH₂ on Bi:10 %In/C; (d) The transition state structure for the *CO and *NH₂ coupling.

after adsorption was also calculated (Fig. S26), and the increase in the density of states near the Fermi level after adsorption indicates a beneficial interaction between the adsorbate and the substrate. The key step for urea production is the coupling of *CO with *NH₂ [24], and the energies of the initial, final and transition states (IS, FS and TS) were calculated (Fig. 6c). The coupling reactions of *CO with *NH₂ is a thermodynamically spontaneous process with a TS energy barrier of only 0.13 eV, followed immediately by a spontaneous exothermic step with $\Delta G = -0.28$ eV, implying easy synthesis of urea. The corresponding transition state structure is shown in Fig. 6d and Fig. S27. For pure Bi/C, the transition state energy barrier of the corresponding step is as high as 0.55 eV (Fig. S28), followed by a spontaneous exothermic step with $\Delta G = -1.71$ eV. Therefore, it is difficult for the reaction of

*CO + *NH₂ → *CONH₂ to proceed smoothly on Bi/C, and even if the coupling is successful, the obtained intermediate *CONH₂ is very stable on the surface of the catalyst, which is not conducive to the second step of the coupling reaction (*CONH₂ + *NH₂ → *CO(NH₂)₂), once again demonstrating the unique effect of In in activating Bi.

4. Conclusion

In summary, the Bi:In/C NPs were designed and synthesized for the electrocatalytic synthesis of urea, where In played a dual role, not only functioning as the active site but also working as an activator to stimulate the activity of Bi, resulting in a remarkable performance of Bi:10 % In/C with average FE of 20.31 % and R_{urea} of 606.38 μg mg⁻¹·h⁻¹ at an

application potential of -0.45 V vs. RHE. The mechanism of the reaction was explored in conjunction with experimental and DFT studies, whereby the $^*\text{NH}_2$ derived from the reduction of NO_3^- and the $^*\text{CO}$ obtained by the reduction of CO_2 as two key intermediates of the reaction were directly coupled to produce C-N bond. This work gives us a deeper understanding to the role of In, while laying the foundation for the subsequent design and construction of highly efficient electrocatalysts.

CRediT authorship contribution statement

Rongxing He conceived the idea and supervised the project. Yini Mao carried out all the experiments, analyzed the data, performed theoretical calculations and wrote the first draft of the manuscript. Yong Jiang, Lirong Zheng and Ming Li assisted in solving the problems encountered during the experiment and participated in theoretical calculations. Qiao Gou, Shengmei Lv, Zuyou Song, Yimin Jiang, Wenbin Wang and Wei Su contributed to the discussion. All authors reviewed and commented on the manuscript before publication.

Declaration of Competing Interest

The authors declare that they have no known competing financial interests or personal relationships that could have appeared to influence the work reported in this paper.

Data Availability

Data will be made available on request.

Acknowledgements

This work was supported by National Natural Science Foundation of China (22109130), the Innovation Research 2035 Pilot Plan of Southwest University (SWU-XDZD22011), the Program for Innovation Team Building at Institutions of Higher Education in Chongqing (CXTDX201601011), Chongqing Municipal Natural Science Foundation (cstc2018jcyjAX0625) and the National Natural Science Foundation of China (22006120).

Appendix A. Supporting information

Supplementary data associated with this article can be found in the online version at [doi:10.1016/j.apcatb.2023.123189](https://doi.org/10.1016/j.apcatb.2023.123189).

References

- [1] J.W. Erisman, M.A. Sutton, J. Galloway, Z. Klimont, W. Winiwarter, How a century of ammonia synthesis changed the world, *Nat. Geosci.* 1 (2008) 636–639, <https://doi.org/10.1038/ngeo325>.
- [2] C. Chen, X. Zhu, X. Wen, Y. Zhou, L. Zhou, H. Li, L. Tao, Q. Li, S. Du, T. Liu, D. Yan, C. Xie, Y. Zou, Y. Wang, R. Chen, J. Huo, Y. Li, J. Cheng, H. Su, X. Zhao, W. Cheng, Q. Liu, H. Lin, J. Luo, J. Chen, M. Dong, K. Cheng, C. Li, S. Wang, Coupling N_2 and CO_2 in H_2O to synthesize urea under ambient conditions, *Nat. Chem.* 12 (2020) 717–724, <https://doi.org/10.1038/s41557-020-0481-9>.
- [3] X. Zhu, X. Zhou, Y. Jing, Y. Li, Electrochemical synthesis of urea on MBenes, *Nat. Commun.* 12 (2021) 4080, <https://doi.org/10.1038/s41467-021-24400-5>.
- [4] F. Barzaghi, F. Mani, M. Peruzzini, From greenhouse gas to feedstock: formation of ammonium carbamate from CO_2 and NH_3 in organic solvents and its catalytic conversion into urea under mild conditions, *Green Chem.* 13 (2011) 1267–1274, <https://doi.org/10.1039/c0gc00674b>.
- [5] Z. Tao, C.L. Rooney, Y. Liang, H. Wang, Accessing organonitrogen compounds via C-N coupling in electrocatalytic CO_2 reduction, *J. Am. Chem. Soc.* 143 (2021) 19630–19642, <https://doi.org/10.1021/jacs.lc10714>.
- [6] Q. Zhao, J.M.P. Martinez, E.A. Carter, Revisiting understanding of electrochemical CO_2 reduction on Cu (111): competing proton-coupled electron transfer reaction mechanisms revealed by embedded correlated wavefunction theory, *J. Am. Chem. Soc.* 143 (2021) 6152–6164, <https://doi.org/10.1021/jacs.lc00880>.
- [7] J. Shao, N. Meng, Y. Wang, B. Zhang, K. Yang, C. Liu, Y. Yu, B. Zhang, Scalable electrosynthesis of formamide through C N coupling at the industrially relevant current density of 120 mA cm^{-2} , *Angew. Chem. Int. Ed.* 61 (2022), e202213009, <https://doi.org/10.1002/anie.202213009>.
- [8] Z. Liu, K. Wang, Y. Chen, T. Tan, J. Nielsen, Third-generation biorefineries as the means to produce fuels and chemicals from CO_2 , *Nat. Catal.* 3 (2020) 274–288, <https://doi.org/10.1038/s41929-019-0421-5>.
- [9] F. Lei, W. Xu, J. Yu, K. Li, J. Xie, P. Hao, G. Cui, B. Tang, Electrochemical synthesis of ammonia by nitrate reduction on indium incorporated in sulfur doped graphene, *Chem. Eng. J.* 426 (2021), 131317, <https://doi.org/10.1016/j.cej.2021.131317>.
- [10] J. Wang, C. Cai, Y. Wang, X. Yang, D. Wu, Y. Zhu, M. Li, M. Gu, M. Shao, Electrocatalytic reduction of nitrate to ammonia on low-cost ultrathin CoOx nanosheets, *ACS Catal.* 11 (2021) 15135–15140, <https://doi.org/10.1021/acscatal.1c03918>.
- [11] W. Wu, Y. Yang, Y. Wang, T. Lu, Q. Dong, J. Zhao, J. Niu, Q. Liu, Z. Hao, S. Song, Boosting electrosynthesis of urea from N_2 and CO_2 by defective Cu-Bi, *Chem. Catal.* 2 (2022) 3225–3238, <https://doi.org/10.1016/j.chemcat.2022.09.012>.
- [12] M. Yuan, H. Zhang, Y. Xu, R. Liu, R. Wang, T. Zhao, J. Zhang, Z. Liu, H. He, C. Yang, S. Zhang, G. Zhang, Artificial frustrated Lewis pairs facilitating the electrochemical N_2 and CO_2 conversion to urea, *Chem. Catal.* 2 (2022) 309–320, <https://doi.org/10.1016/j.chemcat.2021.11.009>.
- [13] M. Yuan, J. Chen, Y. Bai, Z. Liu, J. Zhang, T. Zhao, Q. Shi, S. Li, X. Wang, G. Zhang, Electrochemical C-N coupling with perovskite hybrids toward efficient urea synthesis, *Chem. Sci.* 12 (2021) 6048–6058, <https://doi.org/10.1039/DSC01467F>.
- [14] H. Yin, L. Yang, H. Sun, H. Wang, Y. Wang, M. Zhang, T. Lu, Z. Zhang, W/Mopolyyoxometalate derived electrocatalyst for high-efficiency nitrogen fixation, *Chin. Chem. Lett.* 34 (2023), 107337, <https://doi.org/10.1016/j.ccl.2022.03.060>.
- [15] H. Sun, H. Yin, W. Shi, L. Yang, X. Guo, H. Lin, J. Zhang, T. Liu, Z. Zhang, Porous β -FeOOH nanotube stabilizing Au single atom for high efficiency nitrogen fixation, *Nano Res.* 15 (2022) 3026–3033, <https://doi.org/10.1007/s12274-021-3937-3>.
- [16] M. Jiang, M. Zhu, M. Wang, Y. He, X. Luo, C. Wu, L. Zhang, Z. Jin, Review on electrocatalytic coreduction of carbon dioxide and nitrogenous species for urea synthesis, *ACS Nano* 17 (2023) 3209–3224, <https://doi.org/10.1021/acsnano.2c11046>.
- [17] M. Shibata, K. Yoshida, N. Furuya, Electrochemical synthesis of urea at gas-diffusion electrodes: Part II. Simultaneous reduction of carbon dioxide and nitrite ions at Cu, Ag and Au catalysts, *J. Electroanal. Chem.* 442 (1998) 67–72, [https://doi.org/10.1016/S0022-0728\(97\)00504-4](https://doi.org/10.1016/S0022-0728(97)00504-4).
- [18] M. SHIBATA, K. YOSHIDA, N. FURUYA, Electrochemical synthesis of urea at gas-diffusion electrodes V. Simultaneous reduction of carbon dioxide and nitrite ions with various boride catalysts, Denki Kagaku oyobi Kogyo Butsuri Kagaku 66 (1998) 584–589, <https://doi.org/10.5796/kogyobutsurikagaku.66.584>.
- [19] M. Shibata, N. Furuya, Electrochemical synthesis of urea at gas-diffusion electrodes: Part VI. Simultaneous reduction of carbon dioxide and nitrite ions with various metallophthalocyanine catalysts, *J. Electroanal. Chem.* 507 (2001) 177–184, [https://doi.org/10.1016/S0022-0728\(01\)00363-1](https://doi.org/10.1016/S0022-0728(01)00363-1).
- [20] M. Shibata, K. Yoshida, N. Furuya, Electrochemical synthesis of urea at gas-diffusion electrodes: IV. Simultaneous reduction of carbon dioxide and nitrate ions with various metal catalysts, *J. Electrochem. Soc.* 145 (1998) 2348, <https://doi.org/10.1149/1.1838641>.
- [21] Y. Feng, H. Yang, Y. Zhang, X. Huang, L. Li, T. Cheng, Q. Shao, Te-doped Pd nanocrystal for electrochemical urea production by efficiently coupling carbon dioxide reduction with nitrite reduction, *Nano Lett.* 20 (2020) 8282–8289, <https://doi.org/10.1021/acs.nanolett.0c03400>.
- [22] Y. Liu, X. Tu, X. Wei, D. Wang, X. Zhang, W. Chen, C. Chen, S. Wang, C-bound or O-bound surface: which one boosts electrocatalytic urea synthesis? *Angew. Chem. Int. Ed.* 62 (2023), e202300387 <https://doi.org/10.1002/anie.202300387>.
- [23] S. Zhang, J. Geng, Z. Zhao, M. Jin, W. Li, Y. Ye, K. Li, G. Wang, Y. Zhang, H. Yin, H. Zhang, H. Zhao, High-efficiency electrosynthesis of urea over bacterial cellulose regulated Pd–Cu bimetallic catalyst, *EES Catal.* 1 (2023) 45–53, <https://doi.org/10.1039/d2ey00038e>.
- [24] J. Geng, S. Ji, M. Jin, C. Zhang, M. Xu, G. Wang, C. Liang, H. Zhang, Ambient electrosynthesis of urea with nitrate and carbon dioxide over iron-based dual-sites, *Angew. Chem. Int. Ed. Engl.* 62 (2023), e202210958, <https://doi.org/10.1002/anie.202210958>.
- [25] C. Lv, L. Zhong, H. Liu, Z. Fang, C. Yan, M. Chen, Y. Kong, C. Lee, D. Liu, S. Li, J. Liu, L. Song, G. Chen, Q. Yan, G. Yu, Selective electrocatalytic synthesis of urea with nitrate and carbon dioxide, *Nat. Sustain.* 4 (2021) 868–876, <https://doi.org/10.1038/s41893-021-00741-3>.
- [26] Z. Tao, C.L. Rooney, Y. Liang, H. Wang, Accessing organonitrogen compounds via C-N coupling in electrocatalytic CO_2 reduction, *J. Am. Chem. Soc.* 143 (2021) 19630–19642, <https://doi.org/10.1021/jacs.lc10714>.
- [27] C. Chen, N. He, S. Wang, Electrocatalytic C-N coupling for urea synthesis, *Small Sci. I* (2021), 2100070, <https://doi.org/10.1002/smci.202100070>.
- [28] C.J. Peng, G. Zeng, D.D. Ma, C. Cao, S. Zhou, X.T. Wu, Q.L. Zhu, Hydrangea-like superstructured micro/nanoreactor of topotactically converted ultrathin bismuth nanosheets for highly active CO_2 electroreduction to formate, *ACS Appl. Mater. Interfaces* 13 (2021) 20589–20597, <https://doi.org/10.1021/acsami.1c03871>.
- [29] X.T. Jing, Z. Zhu, L.W. Chen, D. Liu, H.Z. Huang, W.J. Tian, A.X. Yin, Boosting CO_2 electroreduction on bismuth nanoplates with a three-dimensional nitrogen-doped graphene aerogel matrix, *ACS Appl. Mater. Interfaces* 15 (2023) 20317–20324, <https://doi.org/10.1021/acsami.3c02578>.
- [30] N. Zhang, J. Shang, X. Deng, L. Cai, R. Long, Y. Xiong, Y. Chai, Governing interlayer strain in bismuth nanocrystals for efficient ammonia electrosynthesis from nitrate reduction, *ACS Nano* 16 (2022) 4795–4804, <https://doi.org/10.1021/acsnano.2c00101>.
- [31] K. Chen, Z. Ma, X. Li, J. Kang, D. Ma, K. Chu, Single-atom Bi alloyed Pd metallene for nitrate electroreduction to ammonia, *Adv. Funct. Mater.* 33 (2023), 2209890, <https://doi.org/10.1002/adfm.202209890>.

- [32] H. Shen, Y. Zhao, L. Zhang, Y. He, S. Yang, T. Wang, Y. Cao, Y. Guo, Q. Zhang, H. Zhang, In-situ structuring of copper-doped bismuth catalyst for highly efficient CO₂ electrolysis to formate in ampere-level, *Adv. Energy Mater.* 13 (2022), 2202818, <https://doi.org/10.1002/aenm.202202818>.
- [33] C. Lv, C. Lee, L. Zhong, H. Liu, J. Liu, L. Yang, C. Yan, W. Yu, H.H. Hng, Z. Qi, L. Song, S. Li, K.P. Loh, Q. Yan, G. Yu, A defect engineered electrocatalyst that promotes high-efficiency urea synthesis under ambient conditions, *ACS Nano* 16 (2022), <https://doi.org/10.1021/acsnano.2c01956>.
- [34] Y. Mao, Y. Jiang, H. Liu, Y. Jiang, M. Li, W. Su, R. He, Ambient electrocatalytic synthesis of urea by co-reduction of NO₃⁻ and CO₂ over graphene-supported In₂O₃, *Chin. Chem. Lett.* (2023), 108540, <https://doi.org/10.1016/j.cclet.2023.108540>.
- [35] G. Kresse, J. Furthmüller, Efficiency of ab-initio total energy calculations for metals and semiconductors using a plane-wave basis set, *Comput. Mater. Sci.* 6 (1996) 15–50, [https://doi.org/10.1016/0927-0256\(96\)00008-0](https://doi.org/10.1016/0927-0256(96)00008-0).
- [36] G. Kresse, D. Joubert, From ultrasoft pseudopotentials to the projector augmented-wave method, *Phys. Rev. B* 59 (1999) 1758–1775, <https://doi.org/10.1016/j.commatsci.2019.109237>.
- [37] D. Gao, H. Zhou, J. Wang, S. Miao, F. Yang, G. Wang, J. Wang, X. Bao, Size-dependent electrocatalytic reduction of CO₂ over Pd nanoparticles, *J. Am. Chem. Soc.* 137 (2015) 4288–4291, <https://doi.org/10.1021/jacs.5b00046>.
- [38] R. Zhang, Y. Guo, S. Zhang, D. Chen, Y. Zhao, Z. Huang, L. Ma, P. Li, Q. Yang, G. Liang, C. Zhi, Efficient ammonia electrosynthesis and energy conversion through a Zn-nitrate battery by iron doping engineered nickel phosphide catalyst, *Adv. Energy Mater.* 12 (2022), 2103872, <https://doi.org/10.1002/aenm.202103872>.
- [39] C. Huang, A. Xu, G. Li, H. Sun, S. Wu, Z. Xu, Y. Yan, Alloyed BiSb nanoparticles confined in tremella-like carbon microspheres for ultralong-life potassium ion batteries, *Small* 17 (2021), e2100685, <https://doi.org/10.1002/smll.202100685>.
- [40] Y.J. Jang, T.A. Evans, B. Samanta, K. Zeng, M.C. Toroker, K.-S. Choi, A comparative study of Bi, Sb, and BiSb for electrochemical nitrogen reduction leading to a new catalyst design strategy, *J. Mater. Chem. A* 9 (2021) 20453–20465, <https://doi.org/10.1039/dita05327b>.
- [41] W. Yang, Y. Zhao, S. Chen, W. Ren, X. Chen, C. Jia, Z. Su, Y. Wang, C. Zhao, Defective indium/indium oxide heterostructures for highly selective carbon dioxide electrocatalysis, *Inorg. Chem.* 59 (2020) 12437–12444, <https://doi.org/10.1021/acs.inorgchem.0c01544>.
- [42] Y. Xu, K. Ren, T. Ren, M. Wang, M. Liu, Z. Wang, X. Li, L. Wang, H. Wang, Cooperativity of Cu and Pd active sites in CuPd aerogels enhances nitrate electroreduction to ammonia, *Chem. Commun.* 57 (2021) 7525–7528, <https://doi.org/10.1039/d1cc02105b>.
- [43] Y. Wang, A. Xu, Z. Wang, L. Huang, J. Li, F. Li, J. Wicks, M. Luo, D.H. Nam, C. S. Tan, Y. Ding, J. Wu, Y. Lum, C.T. Dinh, D. Sinton, G. Zheng, E.H. Sargent, Enhanced nitrate-to-ammonia activity on copper-nickel alloys via tuning of intermediate adsorption, *J. Am. Chem. Soc.* 142 (2020) 5702–5708, <https://doi.org/10.1021/jacs.9b13347>.
- [44] A. Jha, D.-W. Jeong, J.-O. Shim, W.-J. Jang, Y.-L. Lee, C.V. Rode, H.-S. Roh, Hydrogen production by the water-gas shift reaction using CuNi/Fe₂O₃ catalyst, *Catal. Sci. Technol.* 5 (2015) 2752–2760, <https://doi.org/10.1039/c5cy00173k>.
- [45] H. Hsieh, Y. Chang, W. Pong, J. Pieh, P. Tseng, T. Sham, I. Coulthard, S. Naftel, J. Lee, S. Chung, Electronic structure of Ni-Cu alloys: The d-electron charge distribution, *Phys. Rev. B* 57 (1998) 15204, <https://doi.org/10.1103/PhysRevB.57.15204>.
- [46] M. Zhao, Y. Gu, W. Gao, P. Cui, H. Tang, X. Wei, H. Zhu, G. Li, S. Yan, X. Zhang, Z. Zou, Atom vacancies induced electron-rich surface of ultrathin Bi nanosheet for efficient electrochemical CO₂ reduction, *Appl. Catal. B: Environ.* 266 (2020), 118625, <https://doi.org/10.1016/j.apcatb.2020.118625>.
- [47] S. He, F. Ni, Y. Ji, L. Wang, Y. Wen, H. Bai, G. Liu, Y. Zhang, Y. Li, B. Zhang, H. Peng, The p-orbital delocalization of main-group metals to boost CO₂ electroreduction, *Angew. Chem. Int. Ed. Engl.* 57 (2018) 16114–16119, <https://doi.org/10.1002/anie.201810538>.
- [48] Y. Jiang, H. Liu, Y. Jiang, Y. Mao, W. Shen, M. Li, R. He, Adjustable heterointerface-vacancy enhancement effect in RuO₂@Co₃O₄ electrocatalysts for efficient overall water splitting, *Appl. Catal. B: Environ.* 324 (2023), 122294, <https://doi.org/10.1016/j.apcatb.2022.122294>.
- [49] L. Li, C. Tang, B. Xia, H. Jin, Y. Zheng, S.Z. Qiao, Two-dimensional mosaic bismuth nanosheets for highly selective ambient electrocatalytic nitrogen reduction, *ACS Catal.* 9 (2019) 2902–2908, <https://doi.org/10.1021/acscatal.9b00366>.
- [50] Q. Gong, P. Ding, M. Xu, X. Zhu, M. Wang, J. Deng, Q. Ma, N. Han, Y. Zhu, J. Lu, Z. Feng, Y. Li, W. Zhou, Y. Li, Structural defects on converted bismuth oxide nanotubes enable highly active electrocatalysis of carbon dioxide reduction, *Nat. Commun.* 10 (2019) 2807, <https://doi.org/10.1038/s41467-019-10819-4>.
- [51] B. Nan, L. Li, Y. Li, L. Guo, M. Du, Z. Liu, X. Tao, C. Tian, Z. Liang, Y. Zhang, C. Ma, L. Shen, R. Si, L. Li, Hydrogen-controlled structural reconstruction of palladium-bismuth oxide cluster to single atom alloy for low-temperature CO oxidation, *Appl. Catal. B: Environ.* 334 (2023), 122818, <https://doi.org/10.1016/j.apcatb.2023.122818>.
- [52] A. Dubale, Y. Zheng, H. Wang, R. Hgbner, Y. Li, J. Yang, J. Zhang, N. Sethi, L. He, Z. Zheng, W. Liu, High-performance bismuth-doped nickel aerogel electrocatalyst for the methanol oxidation reaction, *Angew. Chem. Int. Ed.* 59 (2020), <https://doi.org/10.1002/anie.202004314>, 13891–138.
- [53] H. Liu, Y. Jiang, Y. Mao, Y. Jiang, W. Shen, M. Li, R. He, The role of various components in Ru-NiCo alloys in boosting the performance of overall water splitting, *J. Colloid Interface Sci.* 633 (2023) 189–198, <https://doi.org/10.1016/j.jcis.2022.11.091>.
- [54] Y. Jiang, Y. Mao, Y. Jiang, H. Liu, W. Shen, M. Li, R. He, Atomic equidistribution enhanced RuIr electrocatalysts for overall water splitting in the whole pH range, *Chem. Eng. J.* 450 (2022), 137909, <https://doi.org/10.1016/j.cej.2022.137909>.
- [55] Y. Mao, Y. Jiang, H. Liu, Y. Jiang, M. Li, W. Su, R. He, Ambient electrocatalytic synthesis of urea by co-reduction of NO₃⁻ and CO₂ over graphene-supported In₂O₃, *Chin. Chem. Lett.* (2023), 108540, <https://doi.org/10.1016/j.cclet.2023.108540>.
- [56] H. Wang, Y. Jiang, S. Li, F. Gou, X. Liu, Y. Jiang, W. Luo, W. Shen, R. He, M. Li, Realizing efficient C-N coupling via electrochemical co-reduction of CO₂ and NO₃⁻ on AuPd nanoalloy to form urea: key C-N coupling intermediates, *Appl. Catal. B: Environ.* 318 (2022), 121819, <https://doi.org/10.1016/j.apcatb.2022.121819>.
- [57] Z. Wang, Y. Zhou, D. Liu, R. Qi, C. Xia, M. Li, B. You, B.Y. Xia, Carbon-confined indium oxides for efficient carbon dioxide reduction in a solid-state electrolyte flow, *Cell, Angew. Chem. Int. Ed. Engl.* 61 (2022), e202200552, <https://doi.org/10.1002/anie.202200552>.
- [58] N. Meng, X. Ma, C. Wang, Y. Wang, R. Yang, J. Shao, Y. Huang, Y. Xu, B. Zhang, Y. Yu, Oxide-derived core-shell Cu@Zn nanowires for urea electrosynthesis from carbon dioxide and nitrate in water, *ACS Nano* 16 (2022) 9095–9104, <https://doi.org/10.1021/acsnano.2c01177>.